Available online at www.sciencedirect.com

ScienceDirect

Ceramics International 35 (2009) 2357–2366

CERAMICS INTERNATIONAL

www.elsevier.com/locate/ceramint

Structural anomaly and electrical relaxation in $(Na_{2/3}Pb_{1/3})(Mn_{1/2}Nb_{1/2})O_3$ ceramics

Andrzej Molak *, Ewelina Ksepko, Alicja Ratuszna

August Chełkowski Institute of Physics, University of Silesia, Ul. Uniwersytecka 4, PL-40-007 Katowice, Poland

Received 18 November 2008; received in revised form 19 December 2008; accepted 22 January 2009
Available online 13 February 2009

Abstract

The X-ray diffraction patterns of $(Na_{2/3}Pb_{1/3})(Mn_{1/2}Nb_{1/2})O_3$ ceramics were measured within 15–850 K temperature range. The anomaly in the thermal expansion temperature dependence occurred in 250–365 K range. The generalised Cole–Cole model was proposed to describe the measured effective electric permittivity influenced by high electric conduction and the coexistence of two contributions $\varepsilon^*(T,f) = \varepsilon^*_{\text{lattice}} + \varepsilon^*_{\text{carriers}}$ was considered. The analysis of the electric permittivity and conduction exhibited two relaxation processes. The electric conduction relaxation characteristic time values indicated the small polaron mechanism with $\tau_0 \approx 10^{-13}$ s occurring in 240–345 K range and the ionic mechanism with $\tau_0 \approx 10^{-11}$ s involved in the other relaxation occurring in the 320–510 K range. The ionic relaxation process was ascribed to a subsystem of defects, which was weakly interrelated to the anomaly in thermal expansion of the $(Na_{2/3}Pb_{1/3})(Mn_{1/2}Nb_{1/2})O_3$ ceramics. The Gate model was proposed to describe the ionic relaxation mechanism.

Keywords: A. Sintering; B. X-ray methods; C. Electrical conductivity; D. Perovskites

1. Introduction

Recently, the electric properties of the niobate–manganite perovskite $Pb(Mn_yNb_{1-y})O_3$ ceramics were investigated [1–3]. It was shown that complex compounds, e.g. $Pb(Mg_{1/4}Mn_{1/4}Nb_{1/2})O_3$ [4], $Pb(ZrTi)O_3$–$Pb(Mn_{1/3}Nb_{2/3})O_3$ [5,6], $Pb(MgNb)O_3$–$Pb(ZrTi)O_3$–$Pb(Mn_{1/3}Nb_{2/3})O_3$ [7], $BiScO_3$–$PbTiO_3$–$Pb(Mn_{1/3}Nb_{2/3})O_3$ [8], and Mn-doped $Pb(MgNb)O_3$–$PbTiO_3$ [9] exhibited electrical properties suitable for electro-mechanical applications. It was found also that the doping with acceptor Mn ions replacing Nb improved the electro-mechanical properties of such solid solutions [5–9]. It was pointed that the doping with hetero-valence Mn ions may stabilise the oxygen vacancies and facilitate the formation of electric dipoles like V_O–Mn^{k+} that consequently induced electric relaxation phenomena [5,10–14].

However, the sintering of pure perovskite phase $Pb(Mn_yNb_{1-y})O_3$ compounds is difficult and usually multi-component samples are obtained. The occurrence of additional phases, e.g. showing pyrochlore structure or oxides precipitation depends significantly on oxidising–reducing conditions during the synthesis [1–3]. It should be pointed that there is a solubility limit of Mn ions within the Nb sublattice, which can be overcome with suitable co-doping [15–17].

The high electric conduction and electric relaxation phenomena, related to the non-stoichiometry, were reported in the work on the $Pb(Mg_{1/4}Mn_{1/4}Nb_{1/2})O_3$ compound by Modlich et al. [1]. It should be mentioned that the densely packed perfect perovskite structure obstructs an ionic transport. However, pathways for migration of ions are available in defected structures. Hence, the electric relaxation phenomena could be explained in terms of oxygen ions jumping between the vacancies, alike it has been reported for the electric relaxation related to the oxygen non-stoichiometry for various perovskites [10–14]. Moreover, the participation of the Mn and the Nb ions in the relaxation processes ought to be concerned also.

The $(Na_{1-x}Pb_x)(Mn_yNb_{1-y})O_3$ ceramics, containing various proportions of Na and Pb ions, were produced [16–18]. The $(Na_{1-x}Pb_x)(Mn_yNb_{1-y})O_3$ ceramics exhibited high value electric conduction and electric permittivity. The relaxation phenomena were ascribed to the chemical disorder occurring in these compounds [3,16,17].

---

* Corresponding author. Tel.: +48 32 3591186; fax: +48 32 2588431.
E-mail address: andrzej.molak@us.edu.pl (A. Molak).

0272-8842/$34.00 © 2009 Elsevier Ltd and Techna Group S.r.l. All rights reserved.
doi:10.1016/j.ceramint.2009.01.015

The problem whether the anomalies in electric permittivity and conduction ceramics are related either to a structural phase transformation or to a subsystem of defects needs the systematic structural study in a wide temperature range. The aim of this work is to present the XRD structural study and compare them to the electric properties of the $(Na_{2/3}Pb_{1/3})(Mn_{1/2}Nb_{1/2})O_3$ ceramics. We would like also to discuss the role of the Mn ions in the electric conduction.

2. Experimental procedures

The $(Na_{2/3}Pb_{1/3})(Mn_{1/2}Nb_{1/2})O_3$ ceramics were prepared by dry sintering, using a two-stage synthesis process in air [3,16,17,19]. At the first stage, the $Na_{2/3}(Mn_{1/2}Nb_{1/2})O_3$ precursor phase was produced from Na_2CO_3 (Sigma, purity $\geq$99%), Nb_2O_5 (Aldrich, purity $\geq$99.9%) and MnO (Aldrich, purity $\geq$99%) powders prepared in accordance to stoichiometry proportions and calcined at 1223 K. At the second step, the precursor phase constituent was crushed and mixed with the proper amount of PbO (Aldrich, purity $\geq$99.9%). The mixture was sintered at 1173 K for $t = 1$ h. The obtained material was crushed, then milled for 6 h and sieved (<71 μm, Retsch AS200 basic). Any coarse-grained rest of the powder was milled again to obtain the powder finer than 71 μm and then both parts of the powders were joined. The powder was milled dry with use of a zirconia container and balls (Retsch MM200). The powder was pressed at 20 MPa into pellets ($\varphi = 12$ mm, $h \approx 5$ mm). Several trial procedures were carried out to determine the final sintering temperature T_S. It was chosen as $T_S = 1273$ K and 1323 K, combined with the sintering time 2 h, 5 h, and 12 h. The porous ceramics were obtained when they were sintered at 1273 K and when the sintering time was too short. The ceramics sintered at 1323 K in air for 12 h were hard, graphite-black in colour and they were chosen for further analysis.

The determination of the lattice parameters was carried out on powdered samples using an X-ray powder diffractometer SIEMENS D5000. The experimental conditions were: θ–θ geometry, accelerating voltage 40 kV, current 25 mA, the X-ray filtered radiation Cu Kα, $\lambda = 1.54056$ Å, scan method with a step size 0.02° (2θ) and time of counts at every step 13 s. The diffraction pattern was collected in the 10–100° range for 2θ. The chosen lines $\{1\,1\,0\}_p$, $\{2\,0\,0\}_p$, $\{2\,1\,1\}_p$, $\{2\,2\,0\}_p$, and $\{2\,2\,2\}_p$ were measured at stabilised temperature with 50 K and 20 K steps. Measurements were carried out within 15–850 K range with use of two cameras which were changed at room temperature, i.e. an He TTK with closed cooling system for low, and an HTK 1200 for high temperature range. The temperature was stabilised with accuracy of ±1 K.

The X-ray photoelectron spectroscopy (XPS) measurement was carried out on a Multitechnique Electron Spectrometer PHI 5700/660 with Al Kα, radiation (1486.7 eV). A hemispherical mirror analyser measured the energy of the electrons within energy range 0–1400 eV within energy resolution of about 0.3 eV. The real average composition $(Na_{0.68}Pb_{0.38})(Mn_{0.65}Nb_{0.41})O_{2.88}$ was evaluated from the XPS test. Hence, the oxygen deficiency was equal about 4%. In accordance to a simplified ionic picture, the formula for this compound is $(Na^{1+}_{0.68}Pb^{2+}_{0.38})(Mn^{3+}_{0.33}Mn^{4+}_{0.32}Nb^{5+}_{0.41})O^{2-}_{2.88}$ in accordance to the electro-neutrality condition. In the text below we use the nominal composition $(Na_{2/3}Pb_{1/3})(Mn_{1/2}Nb_{1/2})O_3$ of the ceramics. Moreover, a minor phase (the content about 2.5%) detected in the investigated ceramics showed the composition $Na_{0.7}MnO_{2.05}$ [18].

The rectangular samples were cut from the pellets and polished with diamond paste, grade 2000. The surface of the samples was painted with silver paste (Leitsilber 200 from Hans Wolbring GmbH) and dried to obtain electrodes. One can notice that the electrodes became "fired" when the subsequent measurements were carried out at temperature reaching 750 K. Such type of electrode consisted of silver granulates and they would not be blocking for migration of gases from the ceramics surface. Moreover, we carried out only the ac conduction measurement; hence the electrode ought to produce a minor effect on an ionic migration or jumping within the bulk of the samples. The capacitance C and conductivity G were measured with a HP 4263B RLC meter in two or three subsequent cycles of heating and cooling to check repeatability of the results. The measuring frequency was equal to 0.1 kHz, 1 kHz, 10 kHz, 20 kHz, and 100 kHz. The temperature was varied within the range 110–750 K at a constant rate 2 K min^{-1} on heating and cooling with the use of a temperature controller Unipan 680. The data were collected with the use of a PC unit.

The D–E hysteresis loop measurement was carried out with use of a Sawyer–Tower circuit at $f = 20$ Hz and 50 Hz, for the applied electric field up to 4 kV cm^{-1}. The loops did not show any ferroelectric activity at room temperature.

The density evaluated from the XRD data was $\rho_{NOM} = 5.37$ g cm^{-1} for the nominal composition and $\rho_{XPS} = 5.60$ g cm^{-3} in case when the composition determined by the XPS test was taken for evaluation (the elementary cell volume equalled to 63.5 Å^3). The density was measured also as $\rho_E = m/V_{sample} = 4.54$ g cm^{-3} ($d = 0.4$ cm, $\varphi = 1.3$ cm), which were the 81% and 84% of the densities obtained from the XRD data. The effective Young's modulus $C = 1.12 \times 10^{11}$ N m^{-2} was measured by ultrasonic method at $f = 10$ MHz.

3. Results

3.1. XRD analysis

The XRD pattern of the set of the Bragg's diffraction lines, related to the main phase, was indexed with the pseudo-cubic cell Miller indices as shown in Fig. 1.

The parameters of the perovskite-type cell were calculated from the diffraction $\{1\,1\,0\}_p$, $\{2\,0\,0\}_p$, $\{2\,1\,1\}_p$, $\{2\,2\,0\}_p$, and $\{2\,2\,2\}_p$ profiles, fitted by the Pearson VII function using the XP program [20]. This procedure enabled us to determine the position, intensity and split of the multi-component profiles. The split of the main diffraction profiles indicated that the tetragonal distortion of pseudo-cubic cell (with cell parameters $a_p = b_p \neq c_p$) occurred, since it was found that the lines of $\{2\,0\,0\}_p$, $\{1\,1\,0\}_p$, and $\{2\,1\,1\}_p$ type were split in two, as it is presented in Fig. 2, while the line $\{2\,2\,2\}_p$ was the singlet line.

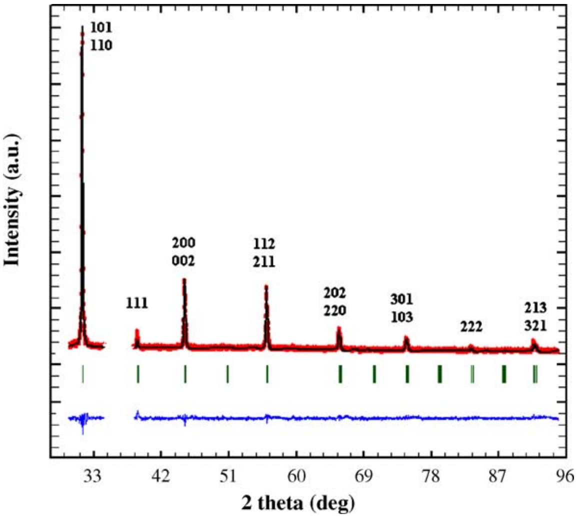

Fig. 1. X-ray powder diffraction pattern of $(Na_{2/3}Pb_{1/3})(Mn_{1/2}Nb_{1/2})O_3$ obtained at room temperature: experimental (circles) and calculated (continuous line) spectrum, vertical ticks for 2θ Bragg positions, the curve on the bottom shows the difference between experimental and spectrum calculated for the *P*4/*mmm* space group.

The trial model of the structure has been proposed as tetragonal with no limiting conditions for the *h k l* reflections. Six space groups: *P*4/*m*, *P*422, *P*42*m*, *P*4*m*2, *P*4*mm*, and *P*4/*mmm* belong to the same diffraction group and they would be considered. The refinement has been performed for a higher symmetry case, i.e. for the centre-symmetric space group *P*4/*mmm*. In the case of the high temperature spectrum, $T_{\mathrm{fit}} = 823$ K, the refinement parameters values were $R_{\mathrm{B}} = 6.82\%$, $R_{\mathrm{F}} = 10.1\%$, and $\chi^2 = 6.70$. In case of the pattern recorded at the $T_{\mathrm{fit}} = 298$ K, the refinement parameters values were $R_{\mathrm{B}} = 7.36\%$, $R_{\mathrm{F}} = 7.53\%$, and $\chi^2 = 6.01$ [18,20–22].

The diffraction spectra obtained at different temperatures, i.e. even in the high and the low temperature ranges were very similar. There were only small variations in intensity of several diffraction lines. The refinement with use of the other symmetry, i.e. the non-centre-symmetric *P*4*mm* space group, was carried out for the pattern, which was obtained at 298 K. It occurred that the refinement parameters values were $R_{\mathrm{B}} = 5.19\%$, $R_{\mathrm{F}} = 7.83\%$, and $\chi^2 = 5.54$. Hence, the difference between the two performed

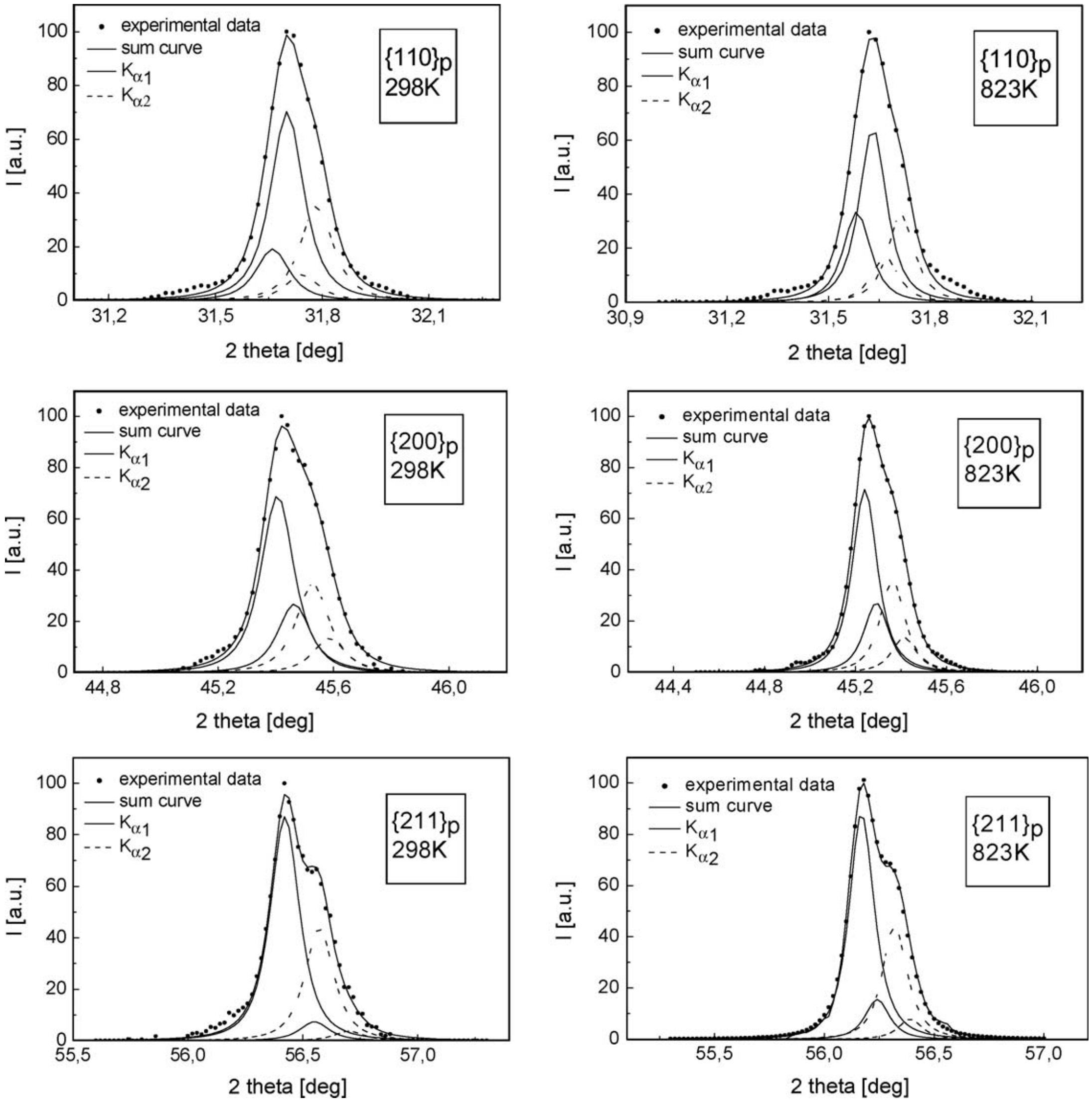

Fig. 2. Split of the chosen main diffraction lines $\{1\,1\,0\}_{p}$, $\{2\,0\,0\}_{p}$ and $\{2\,1\,1\}_{p}$ recorded at 298 K and at 823 K for $(Na_{2/3}Pb_{1/3})(Mn_{1/2}Nb_{1/2})O_3$ (subscript *p* relates to pseudo-cubic perovskite lattice). The $K\alpha_1$ (straight line) and $K\alpha_2$ (dotted line) lines are marked.

refinements occurred insignificant. From such point of view, there was no indication whether the symmetry changes or not between temperature 298 K and 823 K.

Moreover, no independent indications for choosing between specific symmetry for the low temperature range were received from the electrical features of the studied material. Dispersion and anomalies, which related to the electric current relaxation, occurred within wide temperature ranges (see text below). However, no ferroelectric activity was detected at the room temperature. There were found neither frequency independent Curie–Weiss type anomaly, which is a feature of classical electric order phase transition, nor any rounded anomaly in electric permittivity centred on well-defined temperature, which could be ascribed to a diffused phase transition. Similarly, no anomaly in electric permittivity, which could be ascribed to a conventional relaxor phase transition, was distinguished. Hence, there was no evidence for a change in long-range electric order, related to a structural transformation with a macroscopic change in symmetry of the $(Na_{2/3}Pb_{1/3})$ $(Mn_{1/2}Nb_{1/2})O_3$ compound.

The cell parameters *a*, *b*, and *c* temperature dependences in the 15–850 K range are presented in Fig. 3a. The elementary cell volume temperature dependence is drawn in Fig. 3b. The data obtained from the measurement carried out with use of the He TTK and HTK 1200 cameras are distinguished by the full black and open symbols in Fig. 3.

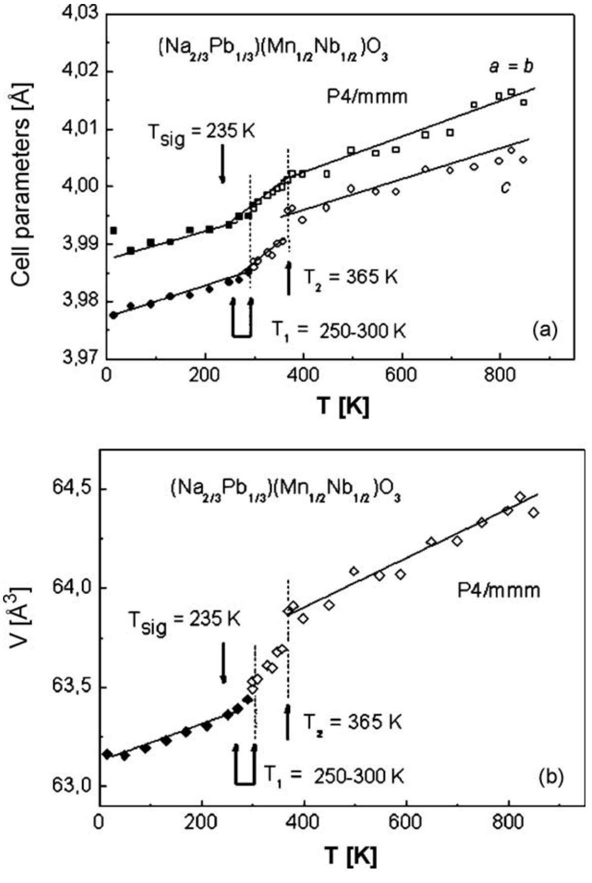

Fig. 3. (a) Cell parameters *a* = *b*, and *c* vs. temperature obtained for $(Na_{2/3}Pb_{1/3})(Mn_{1/2}Nb_{1/2})O_3$ ceramics. (b) The cell volume *V* vs. temperature plot. The T_1 and T_2 denote the changes in the slopes of the cell parameter temperature dependences. The T_{sig} corresponds to the anomaly in electric conductivity.

There are two anomalies in the temperature dependences of $a(T)$, $c(T)$, and $V(T)$. The slope of the lattice constants $a(T)$ and $c(T)$ changes smoothly in the 250–300 K range (noted as T_1 = 250–300 K in Fig. 3). It should be pointed that the upper limit (T = 300 K) of this range accords to the temperature at which the low- and high-temperature cameras (He TTK and HTK 1200) were exchanged. However, the $V(T)$ dependence declines in vicinity of the 250 K. Moreover, the other anomaly visible in vicinity of $T_2 = 365 \pm 5$ K occurs far enough from the room temperature to exclude the effect of the cameras exchange. After that, the temperature T_{sig} = 235 K, related to an anomaly in the electric conductivity temperature dependence, is also marked in Fig. 3. Hence, we deduce that the anomalies which occur in crystal lattice parameters temperature dependences reflect the change in the thermal expansion of the $(Na_{2/3}Pb_{1/3})(Mn_{1/2}Nb_{1/2})O_3$ ceramics. The inter-atomic distances, which were evaluated in case of the XRD patterns obtained at 298 K and 823 K, show that an anisotropy effect manifests in the thermal expansion of the unit cell (Table 1).

3.2. Electric conduction and relaxation

In accordance to the phenomenological model of the small polaron hopping conduction, the electric conductivity of the $(Na_{2/3}Pb_{1/3})(Mn_{1/2}Nb_{1/2})O_3$ ceramics can be separated into thermally activated and the frequency dependent parts. The electric conductivity includes the temperature dependent mobility $\mu \sim T^{-1}$ and the thermally activated dc conduction behaviour:

$$\sigma(\omega, T) = \sigma_{dc}(T) + \sigma_{ac} = \sigma_0 T^{-1} \exp\left(-\frac{E_a}{kT}\right) + A\omega^S \qquad (1)$$

Such dependence was proposed to describe the ac conductivity dispersion in disordered ionic crystals and non-crystalline materials [23,24]. Hence, the electric conductivity multiplied by temperature, $T\sigma$ vs. T^{-1} obtained for the $(Na_{2/3}Pb_{1/3})(Mn_{1/2}Nb_{1/2})O_3$ ceramics, was plotted in Fig. 4.

The equidistant alignment of the $\sigma(T,f)$ plots, measured at f = 0.1–100 kHz, indicated the ac conductivity fulfilled the power law $\sigma_{ac} = A\omega^S$ in high temperature range. The straight-line segments drawn in the $T\sigma(T,f)$ vs. T^{-1} diagram showed that thermally activated processes dominated the electric conductivity

Table 1
Inter-atomic distances between oxygen (in non-equivalent positions I and II) and oxygen, manganese, niobium ions in $(Na_{2/3}Pb_{1/3})(Mn_{1/2}Nb_{1/2})O_3$ perovskite compound. Evaluation carried out for the *P*4/*mmm* symmetry at *T* = 298 and 823 K.

Ions	Inter-atomic distance [Å]	
	T = 298 K	*T* = 823 K
$O_I^{2-} - O_{II}^{-2-}$	2.821(1)	2.830(1)
$O_{II}^{2-} - O_{II}^{2-}$	2.818(8)	2.831(8)
$O_I^{2-} - Mn^{3+}/Nb^{5+}$	1.996(4)	2.032(9)[a]
$O_{II}^{2-} - Mn^{3+}/Nb^{5+}$	1.993(1)	1.701(4)[a]

[a] The minimum values of the distances between the atoms were calculated.

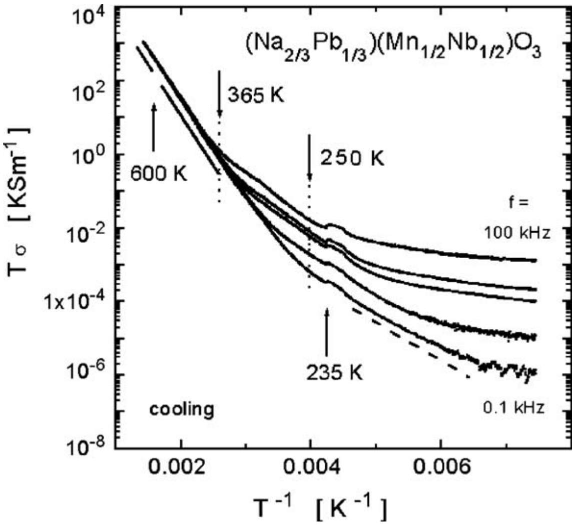

Fig. 4. The electrical conductivity multiplied by temperature, $T\sigma(T,f)$ vs. T^{-1} plots obtained for $(Na_{2/3}Pb_{1/3})(Mn_{1/2}Nb_{1/2})O_3$ ceramics at f = 0.1, 1, 10, 20, and 100 kHz. Activation energy was evaluated in temperature ranges denoted by straight-line segments. The frequency independent anomaly is visible in vicinity of T_{sig} = 235 K. Vertical lines mark the range 250–365 K where anomaly in the thermal expansion occurs.

Table 2
The electric conductivity parameters of $(Na_{2/3}Pb_{1/3})(Mn_{1/2}Nb_{1/2})O_3$ ceramics. The activation energy E_a (accuracy ±0.02 eV) estimated for f = 0.1 kHz within the high and intermediate temperature ranges ΔT. The values of the electric conductivity σ_T measured at T = 600, 400 and 300 K are shown for comparison. The electric conductivity relaxation characteristic time $\tau_{0,M}$ and the relaxation activation energy E_M were calculated from the electric modulus $M''(T,f)$ temperature dependence. The electric conductivity relaxation characteristic times $\tau_{0,B}$ and $\tau_{0,A}$, the activation energies $E_{loss,A}$ and $E_{loss,B}$ were evaluated from loss coefficient derivative $\partial(\log \tan \delta(T,f))/\partial T$ temperature dependence.

E_a [a] (eV)	0.47
σ_{600} (S m^{-1})	4.3×10^{-1}
E_a [b] (eV)	0.44
σ_{400} (S m^{-1})	3.2×10^{-3}
σ_{300} (S m^{-1})	3.3×10^{-5}
E_M [c] (eV)	0.46
$\tau_{0,M}$ [c] (s)	1.3×10^{-11}
$E_{loss,B}$ [d] (eV)	0.52
$\tau_{0,B}$ [d] (s)	1.4×10^{-11}
$E_{loss,A}$ [e] (eV)	0.48
$\tau_{0,A}$ [e] (s)	1.5×10^{-13}

[a] ΔT = 730–600 K.
[b] ΔT = 580–365 K.
[c] ΔT_M = 400–250 K.
[d] ΔT_B = 510–320 K.
[e] ΔT_A = 345–240 K.

within the high and intermediate temperature ranges. The dc conductivity temperature dependence was assumed as the limit of the conductivity measured at frequency f = 0.1 kHz. The activation energy E_a = 0.47 eV (for 600 K < T < 730 K) and E_a = 0.44 eV (for 365 K < T < 600 K) has been evaluated within the high and intermediate temperature ranges, respectively. The electric conductivity value σ_T, measured for f = 0.1 kHz at T = 600, 400 K, and 300 K is shown also in Table 2.

Moreover, an increasing dispersion is visible in the electric conductivity plots within the 235–365 K temperature range. There is a frequency independent bump in vicinity of T_{sig} = 235 K indicating a possibility of a phase transition occurrence. These features correspond to the variation of the cell parameters a, b, c, and V temperature dependences within this temperature range (compare plots in Figs. 3 and 4).

The slight curvature in the conductivity $T\sigma$ vs. T^{-1} plot occurred within the low temperature range. Such a curvature in the plot suggested that the variable range hopping of small polaron model could be concerned in such a case [16,23,24]. The conductivity described with the formula

$$\sigma(T) = \sigma_0 \exp\left(\frac{T_0}{T}\right)^{-1/4} \qquad (2)$$

was fitted numerically below 200 K and the value $T_0 = 5.6 \times 10^8$ K was obtained.

The real part of the electric permittivity dependence on temperature and frequency $\varepsilon'(T,f)$ measured for the $(Na_{2/3}Pb_{1/3})(Mn_{1/2}Nb_{1/2})O_3$ ceramics is shown in Fig. 5a. The main features visible in the $\varepsilon'(T,f)$ plot are the marked dispersion and the frequency dependent step-like anomalies called I and II. The frequency dependent step-like anomalies called A, B, and C occur also in the loss coefficient $\tan \delta(T,f) = \varepsilon''/\varepsilon'$ plot, as a manifestation of relaxation processes related to energy losses (Fig. 5b).

Only a minor anomaly, frequency independent, is visible in the ε and σ plots in vicinity of T_{sig} = 235 K. However, any Curie–Weiss type anomaly that would be a manifestation of the classical electric order phase transition, between paraelectric and ferroelectric phase, was not detected. Such results correspond to the lack of ferroelectric activity determined from the D–E hysteresis loop.

In case of the disordered and highly conducting ceramics samples, when the marked electric conduction dominates and covers electric permittivity peaks, the electric modulus formalism can be effectively applied, since the dc electric conductivity contribution is suppressed in this representation of the data. The electric modulus is evaluated as [3,11,16,19]:

$$M^* = \frac{1}{\varepsilon^*} = (\varepsilon' + i\varepsilon'')^{-1} = M' + iM'' \qquad (3)$$

The imaginary part of the modulus $M''(T,f)$ dependence on temperature obtained for the $(Na_{2/3}Pb_{1/3})(Mn_{1/2}Nb_{1/2})O_3$ ceramics is shown in Fig. 6a. The peak in the $M''(T,f)$ plot shifts to higher temperatures with increasing frequency. Hence, it can be ascribed to the electrical relaxation process. The position of the main peak in the imaginary part of the modulus $M''(T_{peak},f)$ corresponds to the most probable relaxation time at given temperature T_{peak} and frequency f_i. The relaxation times calculated from the condition $\tau_M = (2\pi f_i)^{-1}$ are plotted in Fig. 6b. The relaxation times vary in accordance to the thermally activated dependence:

$$\tau_M = \tau_{0,M} \exp\left(\frac{E_M}{kT}\right) \qquad (4)$$

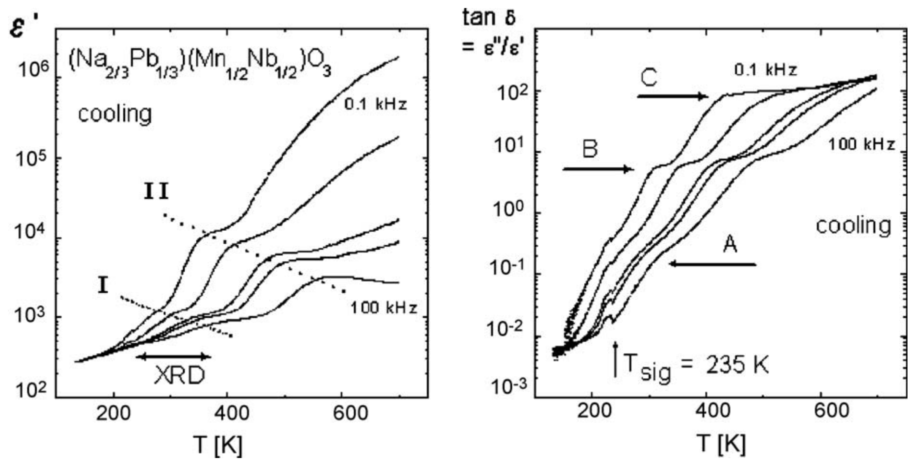

Fig. 5. (a) Electric permittivity real part ε' vs. T plots measured on cooling at f = 0.1, 1, 10, 20, and 100 kHz. Two anomalies called I and II are marked. (b) The loss coefficient tan $\delta = \varepsilon''/\varepsilon'$ vs. T plot. The frequency dependent step-like anomalies A, B and C are marked.

and the numerical fitting with use of Eq. (4) gives the activation energy $E_M \cong 0.46 \pm 0.02$ eV and the electric conductivity relaxation characteristic time $\tau_{0,M} \cong 1.3\ 10^{-11}$ s (Table 2).

It is worthwhile noticing that the electric modulus peak presented in Fig. 6a exhibits slight asymmetry, visible clearly at the higher frequencies. Such two overlapped contributions (pointed by arrows and symbols * and #) indicate the occurrence of two relaxation processes in the investigated material. The parameters of the secondary relaxation process on the left side of the main peak (noted by the mark # in Fig. 6a) could not be evaluated. Due to this hump manifested within narrower temperature range, its activation energy would be slightly higher and corresponding characteristic time shorter.

The use of electric modulus analysis enabled us to determine the parameters of one relaxation process only. Therefore, the other approach has been applied also, in aim to separate the second relaxation. The differential method has been applied to subtract the thermally activated contribution and to receive the relaxation processes [25,26]. For such purpose, the derivative of the loss coefficient,

$$\frac{\partial \log \tan \delta}{\partial T} \qquad (5)$$

was calculated and plotted in Fig. 7a. The temperature dependence showed two series of minima, which were attributed to the relaxation processes (called A and B in Figs. 5b and 7a). The position of a minimum in the $\partial(\log \tan \delta(T,f))/\partial T$ plot allowed to evaluate the most probable relaxation times.

The Arrhenius-type dependences of the relaxation times (Fig. 7b) enabled us to evaluate the activation energy values $E_{\text{loss,A}}$ and $E_{\text{loss,B}}$, and the characteristic times of electric conductivity relaxation $\tau_{0,A}$ and $\tau_{0,B}$, respectively. The results are shown in Table 2. One can notice that the value of the characteristic time $\tau_{0,M}$ obtained from the electric modulus formalism is comparable with the value $\tau_{0,B}$ received from the analysis of derivative of loss coefficient. Moreover, the positions of the main peak in the $M''(T,f_i)$ curve (250–400 K) correspond to the "B" anomaly distinguished in the tan $\delta(T,f_i)$ dependences (compare Figs. 6a, 5b, and 7a and Table 2). It is worthwhile noticing that such correlation is expected due to the relation:

$$\tau_{M''} = \tau_{\varepsilon''}\left(1 + \frac{\Delta\varepsilon}{\varepsilon_\infty}\right)^{-1/a} \qquad (6)$$

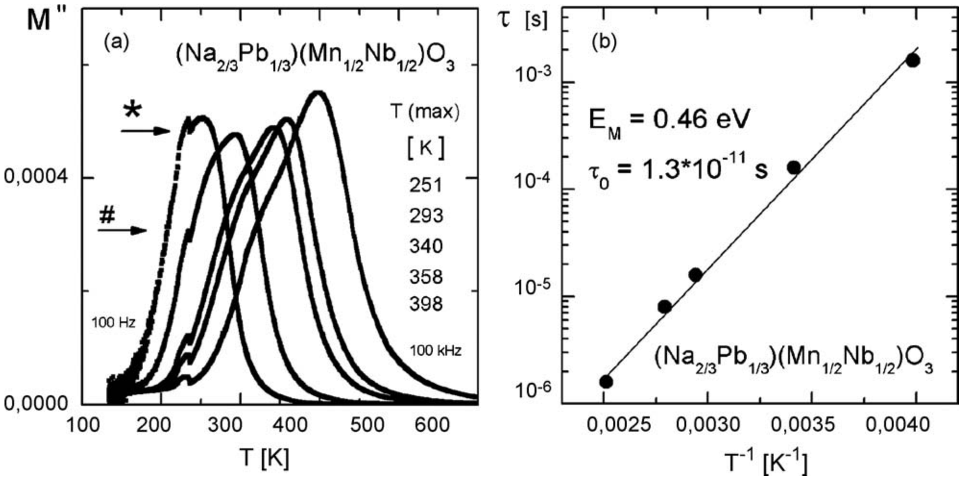

Fig. 6. (a) Imaginary part of electric modulus M'' vs. T, plotted for f = 0.1, 1, 10, 20, 100 kHz. The mark * denotes the primary and the mark # denotes the secondary relaxation process. (b) The Arrhenius dependence plot of the relaxation time τ_M obtained from position of maximum in M'' (T,f).

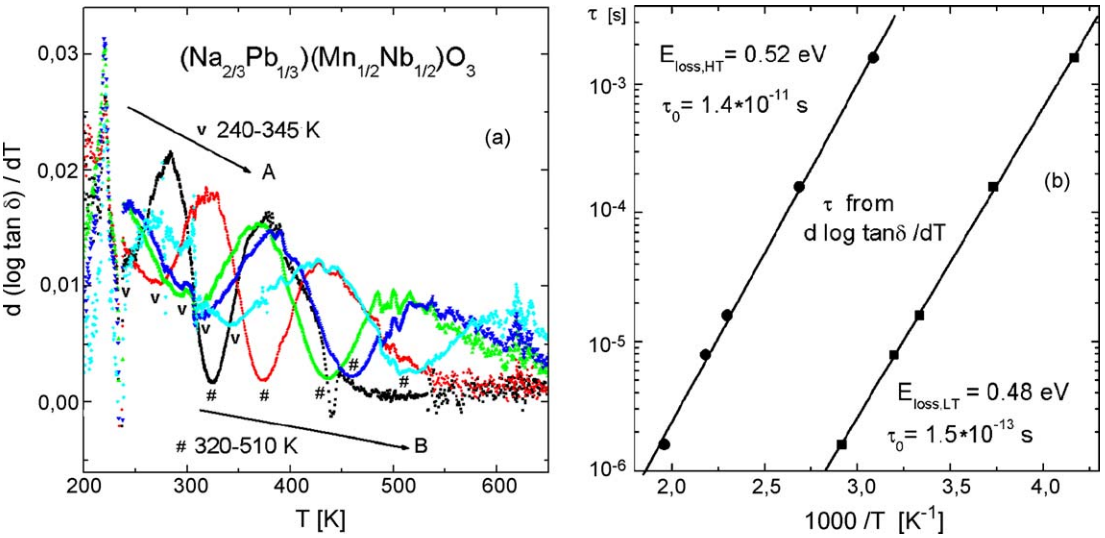

Fig. 7. The derivative of losses coefficient $\partial(\log \tan \delta)/\partial T$ vs. temperature, plotted for $f = 0.1$, 1, 10, 20, and 100 kHz. Two series of minima occurs in the low temperature (240–345 K) and the high temperature (320–510 K) range, ascribed to A and B relaxation processes, respectively. (b) The Arrhenius plots of relaxation times τ obtained from position of minima in $\partial \tan \delta/\partial T$ vs. T plot.

where coefficient a describes the relaxation times distribution. We deduce that the relaxation process described within the electric modulus $M''(T,f)$ approach is equivalent to the process "B" discerned with use of the derivative technique $\partial(\log \tan \delta(T,f))/\partial T$.

4. Discussion

Variation in the thermal expansion of the $(Na_{2/3}Pb_{1/3})(Mn_{1/2}\,Nb_{1/2})O_3$ ceramics reflected lattice behaviour without a change in macroscopic symmetry (see Fig. 3) [27]. Moreover, no classic phase transition related to a change in the electric order was detected. However, it was intriguing that the temperature range, where the thermal expansion coefficient anomaly occurred (250–365 K), overlapped partially with the temperature ranges where the two relaxation processes were observed. There were two processes (called A and B) related to the energy losses which were distinguished from the analysis of the derivative $\partial(\log \tan \delta(T,f))/\partial T$. The process "A" occurred in the temperature range (240–345 K) which was close to the range, where the thermal expansion coefficient anomaly manifested. The process "B" occurred within much wider temperature range (320–510 K). Therefore, we looked for microscopic mechanisms, which could be applied for the description of these two relaxation effects.

It is worth noticing that two relaxation process, described with close values of the τ_0 and slightly lower E_a values were determined for the similar $(Na_{1/2}Pb_{1/2})(Mn_{1/2}Nb_{1/2})O_3$ ceramic compound [16]. Moreover, in the experiment carried out on the as-sintered and oxygenated $(Bi_{0.25}Na_{0.75})(Mn_{0.25}Nb_{0.75})O_3$ samples [19], the relaxation process described with the activation energy value equal $E_a \approx 0.40$ eV has been identified as related directly to the oxygen vacancies. It was also suggested that the other relaxation related to the Mn–V_O electric dipoles. Therefore, the activation energy values obtained for the $(Na_{2/3}Pb_{1/3})(Mn_{1/2}Nb_{1/2})O_3$ ceramics (see Table 3) may correspond to the energy levels originated either from oxygen vacancies or from manganese ions subsystems.

The $(Na_{2/3}Pb_{1/3})(Mn_{1/2}Nb_{1/2})O_3$ ceramics exhibited marked dispersion in the losses, which saturated in the 500–600 K range, reaching the high value $\tan \delta \approx 100$. Correspondingly, the real part of the electric permittivity reached $\varepsilon' \approx 10^6$ at $f = 100$ Hz and only $\varepsilon' \approx 10^3$ at $f = 100$ kHz (see Fig. 5). In case of oxide perovskites, it is generally accepted that the lattice participation in the real part of electric permittivity remains on the $\varepsilon'(T,f) \approx 10^2$ level, and the value of the order of 10^3 is expected in vicinity of phase transition or the lattice instabilities due to high polarizability of oxygen ions.

Hence, the higher values of the measured electric permittivity ought to be explained within the framework of generalised Cole–Cole dependence, where superpositions of the lattice and the space charge carriers responses are considered [28–30]:

$$\varepsilon^*(\omega) = \varepsilon^*(\omega)_{\text{lattice}} + \varepsilon^*(\omega)_{\text{carriers}} \tag{7}$$

where $\varepsilon^*(\omega)_{\text{lattice}}$ is the modified Cole–Cole term and $\varepsilon^*(\omega)_{\text{carriers}}$ is the Almond–West term for ionic conductivity since $\varepsilon^* = i\sigma^*$:

$$\sigma^*(\omega) = \sigma_0\left[1 + \left(\frac{i\omega}{\omega_2}\right)^n\right] \tag{8}$$

Table 3
Strain energy ΔE_S values obtained within Gate model [38–40] where the Mn or Nb ions jump to $V_{Mn/Nb}$ vacancy site via oxygen vacancy V_O. The ionic radii R_{ion} of the mobile ions are taken for six nearest neighbour co-ordination after Shannon [41]. The R_{door} denotes the "doorway" radius calculated from oxygen ions distance obtained from XRD test. Shear modulus values were estimated as $G \approx (3/5)C$, where effective Young's modulus $C \approx 1.12 \times 10^{11}$ N m^{-2} has been obtained from ultrasonic measurement at $f = 10$ MHz.

Mobile ion	R_{ion} (Å)	R_{door} (Å)	R_{door}–R_{ion} (Å)	$G = (3/5)C$ (N m^{-2})	ΔE_S (eV)
Mn^{2+}	0.97	0.58	0.39	0.67×10^{11}	0.78
Mn^{3+}	0.79		0.21		0.18
Mn^{4+}	0.67		0.09		0.03
Nb^{5+}	0.78		0.20		0.16

where σ_0 is dc conductivity, ω_2 is the angular frequency of ionic hopping conductivity, and $0 < n < 1$ (compare Eq. (1)). It would be mentioned that the characteristic frequency of space charge subsystem relaxation is basically independent from the lattice behaviour but could be coupled to the lattice vibration [29]. This generalised Cole–Cole dependence shows that both lattice relaxation and charge carriers relaxation participate not only in the imaginary $\varepsilon''(T,f)$ but also in the real $\varepsilon'(T,f)$ parts of the response to the applied electric field. It is worthwhile noticing that in such a way both the thermally activated and the frequency dependent processes enter the both $\varepsilon'(T,f)$ and $\varepsilon''(T,f)$ parts of the effective electric permittivity.

The XPS study performed on the studied samples exhibited occurrence of the oxygen vacancies. The valence band of the $(Na_{2/3}Pb_{1/3})(Mn_{1/2}Nb_{1/2})O_3$ ceramics is formed from the O 2p states hybridised with the Nb 4d states and the Mn 3d states. Therefore, its features should be similar to those measured in case of $(Na_{1/2}Pb_{1/2})(Mn_{1/2}Nb_{1/2})O_3$ ceramics (see Fig. 8 in Ref. [17]) where a tail of states extends inward the energy gap. Hence, the activation energy of the electric conductivity $E_a = 0.47$ eV and 0.44 eV (see Table 2) is consistent with this feature of the valence band. The activation energies related to the relaxation process, $E_{loss,A} = 0.48$ eV, $E_{loss,B} = 0.52$ eV, and $E_M = 0.46$ eV are close to activation energy E_a of the dc electric conductivity. Therefore, similar energy barriers are involved in the relaxation and in the conduction processes. The electrons thermally generated from oxygen vacancies influence the electric conduction that is commonly accepted in literature, e.g. [10–14,31,32].

It was reported also that the activation energy equal or lower than 1 eV may originate in the perovskite structure either from the oxygen vacancy states [10,12–14,32] or from the Mn-doping ions induced states [33–35]. The type of charge carriers involved in the relaxation can be deduced from the value of characteristic relaxation time of electric conductivity [11,28].

The "A" relaxation occurring within the lower temperature range, with $\tau_{0,A} \approx 10^{-13}$ s can be ascribed to the small polaron process. It may be related either to electron excited from the oxygen vacancy:

$$V_O'' \leftrightarrow V_O' + e^- \tag{9a}$$

or to the Mn ion

$$Mn^{k+} \leftrightarrow Mn^{(k+1)+} + e^- \tag{9b}$$

that results in change in the charge state of the oxygen vacancy or the Mn ion, respectively. The Mn ion, which changes its valence state, remains on its crystallographic site, i.e. it stays within the cage formed by neighbouring ions. However, such ion changes its radius and may shift away (usually about 0.01 Å) from the electron trapped at another site that is followed by the relaxation of the neighbouring lattice [36,37].

The "B" relaxation occurring in the higher temperature range can be ascribed to an atomic or an ionic process, since this process was described by longer characteristic time $\tau_{0,M} \approx \tau_{0,B} \approx 10^{-11}$ s.

We assume that the jumping Mn ions participate in the ionic process of the electric conduction relaxation. Since the perovskite structure is dense, the effective jump of the Mn ion is possible to the vacancy in the Mn/Nb sublattice placed in the next-nearest neighbour position, via an oxygen vacancy placed in between (Fig. 8). Therefore, the bivacancy V_O–$V_{Mn/Nb}$ enables the Mn ion jumping in the defected structure. It should be noticed that the Nb ions might also jump in similar manner. From structural point of view, occurrence of an oxygen vacancy leads to appearance of two square-based pyramids (see Fig. 8), which relax after the jump of the Mn ion (or Nb ion).

In aim to describe the process of Mn ion (or the Nb ion) jump to the $V_{Mn/Nb}$ vacancy, we consider the Gate model [38–40]. Within such approach, the activation energy of ionic conduction relates to the potential energy barrier E_a, which consists of strain energy ΔE_S and electrostatic binding energy ΔE_B. We estimated the strain energy contribution both in case of the Mn

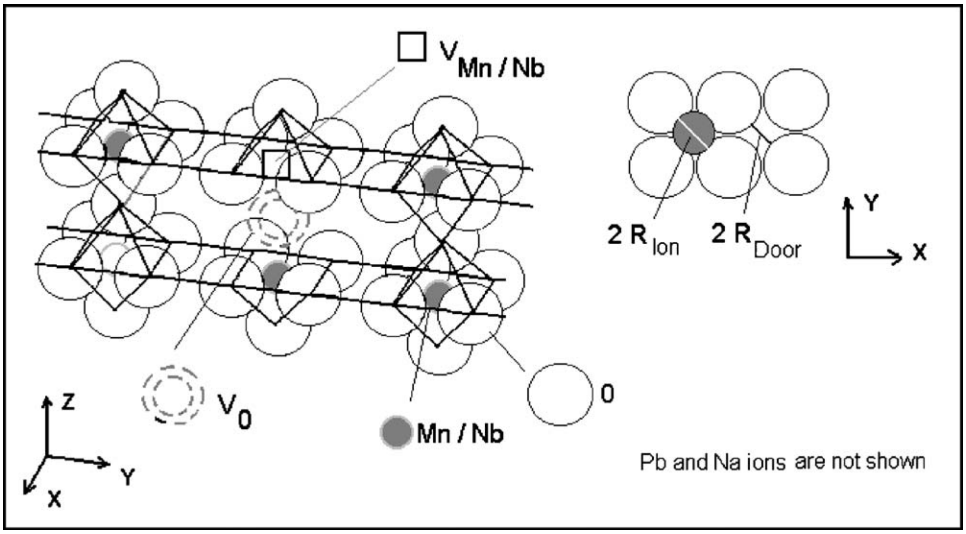

Fig. 8. Schematic representation of the perovskite $(Na_{2/3}Pb_{1/3})(Mn_{1/2}Nb_{1/2})O_3$ network. The Na and Pb ions are not drawn for clarity. The 3D picture, on the left side, shows two square pyramids formed in vicinity of oxygen vacancy. The 2D picture, on the right, shows relations between the oxygen O, manganese Mn or niobium Nb, and the "doorway" radii.

and the Nb ions. The comparison of the strain energy to the activation energy obtained from the electric conductivity analysis (Table 3) would enable us to discern or identify the most probable microscopic mechanism.

The strain energy is expressed by the term:

$$\Delta E_S = 4\pi G R_{door}(R_{ion} - R_{door})^2 \quad (10)$$

where G is shear modulus, R_{door} denotes the "doorway" radius which the mobile ion has to push the surrounding ions away while it jumps to another place, and R_{ion} is radius of the mobile ion.

The R_{door} was evaluated from the lattice constant a and the distance between the oxygen ions in the pyramid base, i.e. from O_{II} to O_{II} distance $d_{II} = (1/2)(\sqrt{2})a = 2.831$ Å (see Table 1 and Fig. 8). Taking the oxygen ion radius as $R_O = (1/2)d_{II} \approx 1.415$ Å, in spherical approximation, the $R_{door} = (1/2)(a - 2R_O) = (3.986 - 2.831$ Å$)/2 = 0.578$ Å. This value is smaller than both Mn^{k+} and Nb^{5+} radii (in $6nn$ co-ordination, after Ref. [41], see Table 3).

The exact experimental value of shear modulus for the $(Na_{2/3}Pb_{1/3})(Mn_{1/2}Nb_{1/2})O_3$ ceramics samples was not known and thus the effective value of Young's modulus $C = 1.12 \times 10^{11}$ N m^{-2} was taken to obtain an approximate G value. The bulk modulus K and elastic constants are related by expression $K = (3\lambda + 2\mu)/3$. In many cases $\lambda = \mu$ [42] and thus shear modulus can be approximated by $G \approx \mu \approx (3/5)K$. Therefore, the evaluation of the strain energy value ΔE_S for the studied ceramics has been carried out using $G \approx (3/5)C$. The obtained values ΔE_S, are shown in Table 3.

The reasonable value of strain ΔE_S should be lower than activation energy value ($E_a = 0.4$–0.5 eV) obtained from the $\sigma(T)$, the $M''(T,f)$, and the tan $\delta(T,f)$ dependencies. Therefore, the jumps of the Mn^{4+} ions, with the $\Delta E_S = 0.03$ eV, are most probable in the jumping and relaxation process because of its smallest radius. Both the Mn^{3+} and the Nb^{5+} ions, for which $\Delta E_S = 0.18$ eV and 0.16 eV, may participate with similar mean probability. The jumps of the Mn^{2+} ions, are impossible from such point of view.

Such result, obtained for the studied $(Na_{2/3}Pb_{1/3})(Mn_{1/2}Nb_{1/2})O_3$ compound, shows that the relaxation, which occurs within high temperature (range B: 280–420 K), can be consistently described with use of the Gate model. Therefore, the Mn ion jump and relaxation between the square-pyramid oxygen cages, via the linking oxygen vacancy, may be considered as alternative for the alone oxygen ion jump and relaxation.

5. Conclusions

- The anomaly in thermal expansion of the cell parameters was determined in the ~235–365 K range, however it was not related to a macroscopic change in symmetry.
- The high value electric permittivity and electric conduction were described within the framework of generalised Cole–Cole dependence, where superpositions of the crystal lattice contribution and the space charge carriers originated from defects contribution were considered.
- Two relaxation processes of the electric conduction of the $(Na_{2/3}Pb_{1/3})(Mn_{1/2}Nb_{1/2})O_3$ ceramics were found. One was related to the small polaron process, the second was ascribed to the ionic process.
- The frequency dependent response of the subsystem of defects, which occurred in a wide temperature range was inter-related to the variation in thermal expansion of the $(Na_{2/3}Pb_{1/3})(Mn_{1/2}Nb_{1/2})O_3$ ceramics.
- The Gate model combined with change in Mn valence state and bivacancy V_O–$V_{Mn/Nb}$ occurrence was proposed in aim to describe the ionic mechanism of electric conduction relaxation.

Acknowledgement

The authors thank Prof. M. Paluch for stimulating discussion.

References

[1] J. Modlich, O. Jarchov, T. Rentschler, A. Reller, U. Bismayer, Synthesis and characterization of Pb(Mg, Mn, Nb)O_3, Solid State Ionics 95 (1997) 131–135.

[2] I.H. Brunskill, R. Boutellier, W. Depmeier, H. Schmid, High-temperature solution growth of $Pb(Fe_{0.5}Nb_{0.5})O_3$ and $Pb(Mn_{0.5}Nb_{0.5})O_3$ crystals, J. Cryst. Growth 56 (1982) 541–546.

[3] A. Molak, E. Talik, M. Kruczek, M. Paluch, A. Ratuszna, Z. Ujma, Characterization of $Pb(Mn_{1/3}Nb_{2/3})O_3$ ceramics by SEM, XRD, XPS and dielectric permittivity tests, Mater. Sci. Eng. B 128 (2006) 16–24.

[4] S. Sharma, R.N.P. Choudary, R. Sati, Structural and dielectric studies of $Pb(Mn_{1/4}Mg_{1/4}Nb_{1/2})O_3$, J. Mater. Sci. Lett. 12 (1993) 530–532.

[5] B.-Sh. Li, G.-R. Li, Q.-R. Yin, Z.-G. Zhu, A.-L. Ding, W.-W. Cao, Pinning and depinning mechanism of defect dipoles in PMnN–PZT ceramics, J. Phys. D: Appl. Phys. 38 (2005) 1107–1111.

[6] Ch.-S. Chen, Chi.-H. Hsu, Ch.-Ch. Chou, Microstructures and piezoelectric properties of microwave-sintered $Pb(Mn_{1/3}Nb_{2/3})_{(0.1)}Zr_{0.52}Ti_{0.38}O_3$ ceramics, Integr. Ferroelectr. 53 (2003) 489–501.

[7] H. Chen, X. Guo, Zh. Meng, Processing and properties of PMMN-PZT quaternary piezoelectric ceramics for ultrasonic motors, Mater. Chem. Phys. 75 (2002) 202–206.

[8] J. Ryu, Sh. Priya, C. Sakaki, K. Uchino, High power piezoelectric characteristics of $BiScO_3$–$PbTiO_3$–$Pb(Mn_{1/3}Nb_{2/3})O_3$, Jpn. J. Appl. Phys. 41 (2002) 6040–6044.

[9] Y.-Y. Chen, S. Hirose, D. Viehland, S. Takahashi, K. Uchino, Mn-modified $Pb(Mg_{1/3}Nb_{2/3})O_3$–$PbTiO_3$ ceramics: improved mechanical quality factors for high-power transducer applications, Jpn. J. Appl. Phys. Part 1. Regul. Papers 39 (2000) 4843–4852.

[10] O. Bidault, P. Goux, M. Kchikech, M. Belkaoumi, M. Maglione, Space-charge relaxation in perovskites, Phys. Rev. B 49 (1994) 7868–7873.

[11] A.K. Jonsher, Universal Relaxation Law, Chelsea Dielectrics Press, London, 1996.

[12] C. Ang, Z. Yu, Z. Jing, P. Lukenheimer, A. Loidl, Dielectric spectra and electrical conduction in Fe-doped $SrTiO_3$, Phys. Rev. B 61 (2000) 3922–3926.

[13] C. Ang, Z. Yu, L.E. Cross, Oxygen-vacancy-related low-frequency dielectric relaxation and electrical conduction in Bi:$SrTiO_3$, Phys. Rev. B 62 (2000) 228–236.

[14] B.S. Kang, S.K. Choi, C.H. Park, Diffuse dielectric anomaly in perovskite-type ferroelectric oxides in the temperature range of 400–700 degrees C, J. Appl. Phys. 94 (2003) 1904–1911.

[15] L.A. Rezhnitchenko, G.A. Geguzina, N.V. Dergunova, Piezoelectric solid solutions based on alkali niobates, Inorg. Mater. 34 (1998) 167–173.

[16] A. Molak, E. Ksepko, I. Gruszka, A. Ratuszna, M. Paluch, Z. Ujma, Electric permittivity and conductivity of $(Na_{0.5}Pb_{0.5})(Mn_{0.5}Nb_{0.5})O_3$ ceramics, Solid State Ionics 176 (2005) 1439–1447.

[17] E. Ksepko, E. Talik, A. Ratuszna, A. Molak, Z. Ujma, I. Gruszka, XPS examination of newly obtained $(Na_{0.5}Pb_{0.5})(Mn_{0.5}Nb_{0.5})O_3$ ceramics, J. Alloys Compd. 386 (2005) 35–42.

[18] E. Ksepko, Thesis, University of Silesia, Katowice, 2006 (in Polish).

[19] A. Molak, M. Paluch, S. Pawlus, J. Klimontko, Z. Ujma, I. Gruszka, Electric modulus approach to analysis of the electric relaxation in highly conducting $(Na_{0.75}Bi_{0.25})(Mn_{0.25}Nb_{0.75})O_3$ ceramics, J. Phys. D: Appl. Phys. 38 (2005) 1450–1460.

[20] A. Kachel, Instruction to XP Program, University of Silesia, Katowice, 1995 (in Polish).

[21] R.A. Young, The Rietveld method, in: IUCr Monographs on Crystallography, 5, International Union of Crystallography, University Press, Oxford, 1995.

[22] J. Rodriguez-Carvajal, Instructions and General Information to Fullproff Program, 1997.

[23] N.F. Mott, E.A. Davies, Electronic Processes in Non-crystalline Materials, Clarendon Press, Oxford, 1971 (Chapters 2 and 7).

[24] A.G. Hunt, Ac hopping conduction: perspective from percolation theory, Philos. Mag. B 81 (2001) 875–913.

[25] M. Wubbenhorst, J. van Turnhout, Analysis of complex dielectric spectra. I. One-dimensional derivative techniques and three-dimensional modelling, J. Non-Cryst. Solids 305 (2002) 40–49;
J. van Turnhout, M. Wubbenhorst, Analysis of complex dielectric spectra. II. Evaluation of the activation energy landscape by differential sampling, J. Non-Cryst. Solids 305 (2002) 50–58.

[26] A. Molak, M. Paluch, S. Pawlus, Z. Ujma, M. Pawełczyk, I. Gruszka, Properties of $(Bi_{1/9}Na_{2/3})(Mn_{1/3}Nb_{2/3})O_3$ analysed within dielectric permittivity, conductivity, electric modulus and derivative techniques approach, Phase Transit. 79 (2006) 447–460.

[27] I.R. Evans, Sh. Tao, J.T.S. Irvine, J.A.K. Howard, Synthesis, crystal structure, and oxide ion conductivity in $Bi_{4.6}Ca_{1.1}VO_{10.5}$, Chem. Mater. 14 (2002) 3700–3704.

[28] R. Coelho, Physics of Dielectrics, Elsevier Sci. Publ. Co., Amsterdam, 1979 (Chapter VI).

[29] D. Ming, J.M. Reau, J. Ravez, J. Gitae, P. Hagenmuller, Impedance-spectroscopy analysis of a $LiTaO_3$-type single crystal, J. Solid State Chem. 116 (1995) 185–192.

[30] K. Majhi, B. Shri Prakash, K.B.R. Varma, Extreme values of relative permittivity and dielectric relaxation in Sr_2SbMnO_6 ceramics, J. Phys. D: Appl. Phys. 40 (2007) 7128–7135.

[31] S.A. Prosandeyev, N.M. Teslenko, A.V. Fisenko, Breaking of symmetry of one-electron orbitals at oxygen vacancies in perovskite-type oxides, J. Phys. Condens. Matter 5 (1993) 9327–9344.

[32] S. Lenjer, O.F. Shirmer, H. Hesse, T.W. Kool, Conduction states in oxide perovskites: three manifestations of Ti^{3+} Jahn–Teller polarons in barium titanate, Phys. Rev. B 66 (2002) 165106.

[33] P. Moretti, F.M. Michel-Calendini, Impurity energy-levels and stability of Cr and Mn ions in cubic $BaTiO_3$, Phys. Rev. B 36 (1987) 3522–3527.

[34] R.L. Gonzales, Y. Leyet, F. Guerrero, J. de Los, S. Guerra, M. Venet, J.A. Eiras, Relaxation dynamics of the conductive processes for $PbNb_2O_6$ ferroelectric ceramics in the frequency and time domain, J. Phys. Condens. Matter 19 (2007) 136218.

[35] J. Kubacki, A. Molak, E. Talik, Electronic structure of $NaNbO_3$–Mn single crystals, J. Alloys Compd. 328 (2001) 156–161.

[36] W.C. Mackrodt, E.-A. Williamson, First-principles Hartree–Fock description of the electronic structure and magnetism of hole and electron states in MnO, J. Phys. Condens. Matter 9 (1997) 6591–6606.

[37] A. Wolska, A. Molak, K. Ławniczak-Jabłońska, J. Kachniarz, E. Piskorska, I.N. Demchenko, I. Gruszka, D.W. Lindle, XANES MnK edge in $NaNbO_3$ based ceramic doped with Mn and Bi ions, Phys. Scripta T115 (2005) 989–991.

[38] J. Kawamura, R. Asayama, N. Kuwata, O. Kamishima, in: T. Sakuma, H. Takahashi (Eds.), Physics of Solid State Ionics, 2006, p. 193.

[39] T. Ishii, Hard-sphere model of activation energy originated in ion size: Gate model, J. Phys. Soc. Jpn. 61 (1992) 2002–2006.

[40] A. Molak, S. Paluch, S. Pawlus, Electrical properties of $Pb(Mn_{1/3}Nb_{2/3})O_3$ ceramics under hydrostatic pressure: relaxation dynamics and its relation to the subsystem of defects, Phys. Rev. B 78 (2008), 134207-1-13.

[41] R.D. Shannon, Revised effective ionic-radii and systematic studies of interatomic distances in halides and chalcogenides, Acta Crystallogr. A 32 (1976) 751–767.

[42] J.-P. Poirier, Introduction to the Physics of the Earth's Interior, Cambridge University Press, Cambridge, 1991 (Chapter 6).